



Denudation outpaced by crustal thickening in the eastern Tianshan

Julien Charreau, Dimitri Saint-Carlier, Stephane Dominguez, Jérôme Lavé, P. Blard, Jean-Philippe Avouac, Marc Jolivet, Yan Chen, Shengli Wang, David. Nathan Brown, et al.

► To cite this version:

Julien Charreau, Dimitri Saint-Carlier, Stephane Dominguez, Jérôme Lavé, P. Blard, et al.. Denudation outpaced by crustal thickening in the eastern Tianshan. *Earth and Planetary Science Letters*, 2017, 479, pp.179-191. 10.1016/j.epsl.2017.09.025 . insu-01610154

HAL Id: insu-01610154

<https://insu.hal.science/insu-01610154v1>

Submitted on 28 Nov 2019

HAL is a multi-disciplinary open access archive for the deposit and dissemination of scientific research documents, whether they are published or not. The documents may come from teaching and research institutions in France or abroad, or from public or private research centers.

L'archive ouverte pluridisciplinaire **HAL**, est destinée au dépôt et à la diffusion de documents scientifiques de niveau recherche, publiés ou non, émanant des établissements d'enseignement et de recherche français ou étrangers, des laboratoires publics ou privés.

The Tianshan range, an example of an immature orogenic wedge? Evidence from active deformation and denudation rates within the intermontane basins

Julien Charreau¹, Dimitri Saint-Carlier¹, Stéphane Dominguez², Jérôme Lavé¹, Pierre-Henri Blard¹, Jean-Philippe Avouac³, Marc Jolivet⁴, Yan Chen⁵, ShengLi Wang⁶, Nathan David Brown⁷, Luca Claude Malatesta³, Edward Rhodes⁷, and ASTER Team^{8*}

¹ Université de Lorraine, CRPG, UMR 7358 CNRS-UL, 15 rue Notre Dame des Pauvres, 54501 Vandœuvre lès Nancy, France

² Université de Montpellier, Géosciences Montpellier, UMR 5243, Place E. Bataillon, 34095 Montpellier Cedex 5, France

³ California Institute of Technology, Division of Geology and Planetary Sciences, 1200 E California Blvd, Pasadena CA 91125, United States

⁴ Université de Rennes, Géosciences Rennes, UMR 6118, Campus de Beaulieu 35042 Rennes, France

⁵ Université d'Orléans, Institut des Sciences de la Terre d'Orléans, UMR 7327, Campus Géosciences, 45071 Orléans, France

⁶ Nanjing University, Department of Earth and Sciences, Nanjing, China

⁷ University of California, Department of Earth, Planetary and Space Sciences, Los Angeles, California 90095-1567, United States

⁸ Université Aix-Marseille, CNRS-IRD-Collège de France, UM 34 CEREGE, Technopôle de l'Environnement Arbois-Méditerranée, 13545 Aix-en-Provence, France

* M. Arnold, G. Aumaître, D.L. Bourlès, K. Keddadouche

Keywords: Tianshan; ¹⁰Be exposure dating; shortening rates; Intermontane basin; Bayanbulak basin; relief dynamics; mountain building; active tectonics

ABSTRACT

The modern Tianshan mountain range resulted from the reactivation of a Paleozoic orogenic belt in response to the India/Asia collision and today the range exhibits high topography, tectonically active forelands, and intermontane basins. The distribution of crustal shortening across the range is likely controlled by inherited Paleozoic structures.. Based on quantitative morphotectonic observations and age constraints derived from cosmogenic ¹⁰Be dating, single-grain post-infrared infrared stimulated luminescence (p-IR IRSL) dating and modeling of fault scarp degradation, we have quantified the deformation in the Nalati and

Bayanbulak intermontane basins in the central Eastern Tianshan. Our results indicate that at least 1.4mm/yr of horizontal crustal shortening is accommodated within these two basins. This shortening represents a significant portion ($>15\%$) of the 8.5 ± 0.5 mm/yr total shortening rate across the entire range at this longitude. Accordingly, the Eastern Central Tianshan is thickening at a mean rate of ~ 1.4 mm/yr, a rate that is significantly higher than the average denudation rate of 0.14 mm/yr derived from our cosmogenic analysis. This discrepancy suggests that the Tianshan range has not yet reached a steady topography and remains in a transient state of topographic growth, most likely due to the arid climate, which limits the denudation rates.

1. INTRODUCTION

Intracontinental orogenic belts typically form single or double vergent prisms that grow from a combination of frontal accretion and underplating (e.g. Willett et al., 2001). In the presence of denudation, a topographic steady-state can be reached in which denudation balances crustal thickening (J. Avouac and Burov, 1996; Dahlen and Suppe, 1988; Willett et al., 2001). This could result from either crustal shortening of the internal part of the range or underplating due to an accumulation of material which is then thrust under the wedge. The resulting balanced topography generally has a simple asymmetric triangular shape, with steeper slopes on the windward side of the range (Willett et al., 2001).

Here, we investigate the Eastern Tianshan in central Asia (Fig. 1), whose topography differs from these classical profiles (Fig. A) even though it is one of the largest and most active intracontinental orogenic belts in the world. The range is composed of a series of elevated ranges (> 4000 m) separated by very large E–W striking intermontane basins such as the Yili, Bayanbulak, Nalati, Turpan and Yanqi basins (Fig. 1). How this particular topography is growing, and especially whether or not it has reached a steady state, are questions that remain unresolved.

Present-day shortening rates, derived from GPS measurements across the entire range, reach 20 mm/yr in the western Tianshan and decrease progressively eastward, to a value of 8.5 ± 0.5 mm/yr at the longitude of this study and to even lower rates further east (e.g. Reigber et al., 2001; Yang et al., 2008). Because of the presence of inherited Paleozoic structures, this shortening is not focused on the boundaries but is instead distributed across the entire range, and significant evidence for active deformation is observed within the central part of the range (Jolivet et al., 2010; Poupinet et al., 2002; Thompson et al., 2002; Wu et al., 2014). In the eastern part of the range, the amount and rate of internal deformation remains poorly constrained (Jolivet et al., 2010; Wu et al., 2014). Recent denudation rates on both sides of the range are relatively low (0.2–0.4 mm/yr) (Guerit et al., 2016; Jolivet et al., 2010; Puchol et al., 2016). Over the long term, because Cenozoic denudation is very limited, even low temperature thermochronometers are of limited use in documenting the recent exhumation history of the range, except for within the most active zones (Dumitru et al., 2001; Jolivet et al., 2010). To better understand how the Tianshan is growing and to determine whether this range has reached steady-state topography, more quantitative constraints on the distribution of deformation across the range and its evolution through time, as well as estimates of the associated denudation, are required, especially in the inner regions.

This study focuses on the Central Eastern Tianshan and investigates recent tectonics in the Bayanbulak and surrounding Nalati and Yili intermontane basins (Fig. 1). Evidence for active tectonics in this region has been reported but is poorly quantified. Here, we use different techniques to quantify deformation and denudation rates. We demonstrate that crustal thickening outpaces denudation and conclude that, despite its long geological history and high topography, the Tianshan range is still in an early stage of topographic growth due to the extremely low erosion rates in the region.

2. GEOLOGICAL SETTING AND EVIDENCE FOR ACTIVE DEFORMATION IN THE INTERMONTANE BASINS

After a long Paleozoic geological history, the numerous intermontane basins were created by a post-orogenic phase of transtensive deformation during the Permian to Late Triassic (Charvet et al., 2007; Jolivet et al., 2010). These basins are still partially preserved, though the range was strongly rejuvenated and shortened in the Late Cenozoic in response to the India/Asia collision (e.g. Tapponnier and Molnar, 1979), which continues today.

The Bayanbulak, Nalati and Yili basins are large intermontane troughs, situated ~1500 to ~2400 m.a.s.l. (Fig. 1B) and surrounded by high elevation ranges with peaks at > 4000 m composed mainly of Paleozoic meta-sedimentary and igneous basement (Fig. 1C).

The Bayanbulak basin is located between the South Tianshan range to the south and the Narat range to the north. The northern edge of the basin exhibits clear evidence for recent deformation along several northward-dipping E–W trending parallel stepped faults and associated ~10 km long topographic scarps (Figs. 1C, 2, 3 and 4). These faults deform numerous alluvial fan surfaces that were abandoned by southward flowing rivers that drain the Narat range (Figs. 2 and 3).

Located to the north, the Nalati basin is a relatively small basin trapped within the northern piedmont of the Narat Range and bound to the north by the >2000 m high Nalati range. At least two parallel reverse faults, trending roughly E–W and dipping to the south, can also be mapped within this basin (Fig. 5). The first lies at the base of the main reliefs of the Narat Range and affects Quaternary glacial deposits. The second of these faults clearly offsets the most recent alluvial sediments of the Nalati Basin (Fig. 5).

The Yili basin lies at a lower elevation north of the Nalati range and is limited to the north by the Borohoro range. The basin is relatively narrow in the east but rapidly widens toward the west in Kazakhstan. High E–W striking topographic steps can be observed along its southern border (Fig. 5D). The nearby E–W flowing Yili river located at the center of the

basin might also have left E–W striking terrace risers, and thus the tectonic origin of the topographic steps might be questioned. However, the presence of reverse and convex slopes is suggestive of a tectonic origin.

3. SHORTENING ESTIMATES

3.1 Method

To quantify the amount of shortening across these active thrust faults, we determined the vertical throw by measuring the vertical offset of the morphological markers. A Trimble DGPS topographic device was used to acquire high resolution topographic measurements of the markers. The elevation was then corrected from the regional slope estimated at each study site, and the offset was measured directly on the corrected profiles. We considered a conservative uncertainty of 15 % on the total vertical throw to account for morphological roughness and horizontal advection of the regional slopes. The vertical throw was then converted into a horizontal component of slip using the fault dip angle. Because of poor outcrop conditions and the lack of subsurface geophysical data, we also assumed a fault dip angle of $35\pm 10^\circ$ based on outcropping faults measured in the east of the Bayanbulak basin by Jolivet et al. (2010) and Wu et al. (2014). We assume that all of the faults studied are pure thrust faults as they strike approximately perpendicular to the azimuth of geodetic shortening across the range (Fig. 1) and because the strike-slip component appears to be mostly second order, at least in the basins studied (Wu et al., 2014).

3.2 Study sites and results

In the Bayanbulak basin, five sites were analyzed, numbered 1 to 5 from south to north. Site BBK1 is located roughly ~20 km south of Bayanbulak city, where the Kaidu River entrenches a large E–W trending anticline, abandoning two levels of fluvial terraces (Fig. 2).

The anticline is bordered to the south by a north-verging thrust (F1) that has deformed the abandoned terraces. To the northwest, site BBK2 lies at the base of the Narat Range, where a second E–W trending fault (F2) offsets a large alluvial fan that was later overlain by a younger fan at the base of the fault (Fig. 2). Two sites (BBK3 and BBK4) located roughly 25 km east of BBK2 were also studied at the base of the Narat range (Figs. 1c and 3). Here, three E–W fault scarps (F3, F4 and F5) are intersected by southward flowing rivers (Fig. 3). At site BBK3, three other fault scarps (F3, F4 and F5) offset four terrace levels (T1 to T4, Figs. 3 A, B and C). Site BBK4 is located ~4 km further east along the strike of fault F3 where two terraces are affected by this fault (Figs. 3D and E). Finally, site BBK5 is located in the eastern part of the basin within a large north–south oriented valley that was entrenched within the Narat range by a tributary of the Kaidu river, which flows toward the center of the Bayanbulak basin (Figs. 1 and 4). Here, one major east–west striking thrust fault (F6) offsets the alluvial deposits of the tributary. We also studied a sixth site (site N) in the Nalati basin on the northern side of the Narat range (Figs. 1 and 5). Here, large recent alluvial fans trapped within the basin have been offset by a major 25 km long E–W striking fault (Fig. 6). In the Yili basin, despite strong evidence for active tectonics, the recent deposition of thick loess (e.g. Yi et al., 2012; Song et al., 2012; Long et al., 2014) has likely changed the original geometry of the morphological markers. We were therefore unable to identify any sites where an accurate estimation of the topographic uplift would be possible.

The measured vertical throw, derived fault slip, and horizontal shortenings, together with their uncertainties, are listed in Table 1 for each of the study sites and faulted terraces. Note that at site BBK3 (Fig. 3), we focused our analyses on terraces T2, T3 and T4 because the offset of terrace T1 was too small to be quantified precisely. We also summed the offsets of faults F4 and F5 at this site as the surface traces of these faults are very close together, suggesting that the two faults probably merge at depth. Moreover, as the terrace level cannot

be traced south of F3, the uplift measured across this particular fault should be considered a minimum value. Finally, the offset of terrace T4 is only visible across fault F5 and has not been preserved elsewhere. Note also that at site BBK4, the small pressure ridges affecting terraces T1 and T2 on the left bank of the gully (Fig. 3E) are not continuous along strike and can be considered a second order feature. As such, we neglected these small ridges and quantified the terrace uplift by considering their large-scale geometries. In the Bayanbulak basin, vertical offsets preserved by offset geomorphic markers are typically of a few meters to a few tens of meters. In the Nalati basin, the fault scarps can be much higher, reaching ~45 m.

4. DATING OF MORPHOLOGICAL MARKERS

4.1 Cosmogenic depth profile inversion

4.1.1 Principle and theory

The abandonment ages of most of the alluvial surfaces were inferred from the depth distribution of cosmogenic isotope concentrations (e.g. Gosse and Phillips, 2001). In the general formula of Lal (1991) used to describe the change in ^{10}Be concentration (C) as a function of depth (Z), the concentration of ^{10}Be also depends on the time since initial exposure of the surface (in this case, the abandonment of the terrace surfaces) and on the erosion rate of the surface of the terrace. During the Late Quaternary, the region experienced strong aridification, which led to widespread deposition of loess over the pre-existing alluvial deposits (Long et al., 2014; Song et al., 2012; Yi et al., 2012). Thus, erosion of the terraces was probably very limited. Alternatively, the loess layer may have shielded the underlying alluvial sediments. To account for potential deposition of loess and/or soil after abandonment of the terraces, we modified the general equation of Lal (1991) as follows:

$$C(z, \varepsilon, t) = \overline{C_0} \cdot e^{-\lambda \cdot t} + \sum_{i=n, m_1, m_2} \frac{P_i}{\frac{\rho \cdot B}{\Delta_i} + \lambda} \cdot e^{\frac{-\rho \cdot z}{\Delta_i}} \cdot \left(1 - e^{-\left(\lambda + \frac{B \cdot \rho}{\Delta_i} \right) \cdot t} \right) \quad (1)$$

where B is a "negative" denudation rate (Braucher et al., 2000) that represents the accumulation rate or burial rate since terrace abandonment; t represents the time since initial exposure of the surface (in this case, the abandonment of the terrace surface); C_0 is the average cosmogenic inheritance (in atoms/g); λ is the decay constant of ^{10}Be , equal to $\ln(2)/\mathcal{T}_{1/2}$ where $\mathcal{T}_{1/2}$ is the half-life (1.387 Ma) (Chmeleff et al., 2010; Korschinek et al., 2010); n , m_f , and m_s refer to the neutrons, fast muons and slow muons, respectively; Δ is the attenuation length of neutrons, slow muons or fast muons (~ 160 , ~ 1500 , ~ 4320 g/cm²) (Braucher et al., 2011); P_i is the local production rate (at g⁻¹ yr⁻¹) for the different particles; and ρ is the soil density (g/cm³).

This formula does not apply to the sediments deposited during this sedimentation phase. To compute the concentration in these later deposits, it is necessary to assume that the exposure time of each sample is dependent on its depth ($t = z/B$). The equation then becomes (Guralnik et al., 2011):

$$C(z, B) = \overline{C}_0 \cdot e^{\frac{\lambda \cdot z}{B}} + \sum_{i=n, m_f, m_s} \frac{P_i}{\frac{\rho \cdot B}{\Delta_i} + \lambda} \cdot e^{\frac{-\rho \cdot z}{\Delta_i}} \cdot \left(1 - e^{\left(\frac{\lambda}{B} + \frac{\rho}{\Delta_i} \right) \cdot z} \right) \quad (2)$$

We assume that the few tens of centimeters of loess covering the terraces (Fig. 2) accumulated at a constant rate after terrace abandonment. This assumption is consistent with OSL dating of thick loess sections in the Yili basins (e.g. Song et al., 2012; Long et al., 2014; Yi et al., 2012). Additionally, we calculated end-member age estimates by assuming 1) instantaneous deposition of the entire loess layer immediately after terrace abandonment (maximum age), and 2) very recent deposition of the entire loess layer, meaning that this did not affect the cosmogenic depth profile in the underlying alluvium (minimum age; attenuation in the loess is ignored in such a case).

To derive the exposure ages from the depth profiles, we followed a Monte Carlo inversion procedure that tests thousands of parameter combinations to find the best fitting solution by minimizing the difference between the model and the data (e.g. Braucher et al., 2009; Saint-Carlier et al., 2016).

The local ^{10}Be production rates for neutrons, fast muons and slow muons were scaled for local latitude and altitude according to Stone (2000), and the local atmospheric pressures were extracted from the ERA40 dataset (Uppala et al., 2005). In this study, we used the SLHL (see level high latitude) production rate of $3.9 \pm 0.1 \text{ at g}^{-1} \text{ yr}^{-1}$ (compiled by Balco et al. (2009) and revised by Braucher et al. (2011) to include the slow and fast muon contributions). The slow ($0.01 \text{ at g}^{-1} \text{ yr}^{-1}$) and fast ($0.034 \text{ at g}^{-1} \text{ yr}^{-1}$) muonic production rates were derived from Braucher et al. (2011). Because the study region is located at high elevation, snow cover could have an impact on the cosmogenic production rate. However, the area is in fact very arid and snow cover is limited to an average of $\sim 12 \text{ cm}$ during 139 days per year (Yang and Cui, 2005). Moreover, because snow has a very low density ($\sim 0.1 \text{ g cm}^{-3}$), its impact on production rate evaluations can be neglected. Alluvium density was estimated by analyzing photographs of the different outcrops in order to determine the relative proportions of cobbles ($\text{Ø} > 1\text{-}2 \text{ cm}$) and sand to fine gravels. The bulk density was then calculated by attributing densities of $2.7 \pm 0.1 \text{ g/cm}^3$ to the cobbles and $1.9 \pm 0.1 \text{ g/cm}^3$ to the sand to fine gravels (Hancock et al., 1999).

4.1.2 Sampling

Sampling for cosmogenic depth profile analyses (Fig. 6 and A) was restricted to the Bayanbulak basin where the loess cover is thinnest. In the Nalati and Yili basins the loess layers are much thicker and the timing of their deposition might be highly variable (e.g. Song et al., 2012; Long et al., 2014; Yi et al., 2012), meaning that the shielding effect cannot be

233 properly corrected for. In the Bayanbulak basin, the sampling sites were carefully selected
234 and the outcrops refreshed to avoid any recent re-exposure (Fig. B). At all sites selected for
235 dating, samples were collected from the surface and from different depths in order to measure
236 the ^{10}Be concentrations in the quartz. We preferentially sampled sand at depth for the
237 cosmogenic dating, however pebbles and cobbles were collected at points near to the surface
238 because the grain size was too coarse and the proportion of sand too low for collection of
239 adequate quantities of sand (Figs. 6 and A in the online depository). At site BBK4, we
240 sampled the highest alluvial surface (T2), which corresponds to a fan deposit. The deposit is
241 composed of mixed sediment, ranging from sand to cobble in grain size, and is quite
242 homogenous across the full thickness that was excavated. The entire site is covered by
243 grassland, in which low vegetation grows on a 15 cm thick soil. Sampling was performed
244 along the most recently eroded part on the modern riser of an incising river (Fig. B) down to
245 ~9.5 m below the surface (Fig. B). In addition, four sand samples were taken at between 35
246 and 200 cm depth and three amalgamated cobbles samples were collected within the 15 cm of
247 soil (Fig. B). At site BBK3, we sampled two alluvial surfaces at different locations: one at T2
248 and one at T3 (Fig. 2). Site BBK3-T2 was sampled on the active riser of the river, and we
249 extracted 4 sand samples at between 45 and 400 cm depth and 2 amalgamated cobble samples
250 that were mixed in the 25 cm of loess deposit (Fig. B). As the BBK3-T3 surface is located far
251 from the river, we dug a hole and collected 5 sand samples at between 30 and 170 cm depth.
252 Both of the BBK3 terraces sampled are composed of mixed sediments ranging from sand to
253 boulder in size. Site BBK1, located in the south, presents two terrace levels that cut through
254 an antecedent anticline. The highest terrace (T2) at site BBK1 was covered by 30 cm of over-
255 bank deposit and 45 cm of loess at the top. We took five samples (between 80 and 280 cm
256 depth) of the sandy fraction within the alluvial material of the terrace (composed of sand to
257 cobble sediment), two samples from the silty part of the terrace and one from the loess part

(Fig. B). To collect these samples, we dug a 280 cm deep trench in the terrace riser. The details of the sample treatment and analyses are provided in the online repository.

4.1.3 Results of the cosmogenic depth profile inversions

The results of the cosmogenic analyses are reported in Table A in the online repository. The cosmogenic depth profiles studied all show a classic exponential decrease in ^{10}Be concentration. The inversions of these profiles (Fig. 6), assuming continuous sedimentation, constrain the mean exposure time of the terraces to 64 ± 6 ka, 22 ± 2 ka, $91\pm11/9$ ka and $88\pm7/6$ ka for the sites BBK4, BBK3-T2, BBK3-T3 and BBK1-T2, respectively (Fig. 6). The hypothesized end-member ages, which assume either instantaneous deposition of loess after terrace abandonment or only recent deposition, bracket these ages to within less than 20 % error (Fig. 6).

4.2 Single-grain p-IR IRSL dating of loess deposits

To better constrain the age of the loess deposit shielding the cosmogenic dated surfaces in the Bayanbulak basin, we also carried out single-grain post-infrared infrared stimulated luminescence (p-IR IRSL) dating of K-feldspar grains (e.g. Thiel et al., 2011). We collected one sample at site BBK1 (Fig. 1) where terrace T2 is covered by a 70 cm thick layer of loess. The sample was taken immediately above the alluvial deposits at the base of the loess layer (~70 cm below the surface). The silty/loess material was sampled in a metallic pipe and rapidly shielded using black tape. The detail of the sample treatment and measurement are given in the Online repository.

The fading-corrected age of the sample constrains the abandonment age of BBK1-T2 to 38.7 ± 4.9 ka (Table B and Fig. C). This sample was collected from within the silt/loess cover that caps the terrace deposit and therefore provides a minimum estimate for the timing

of terrace abandonment. The IRSL age of ~38 ka is significantly younger than the age derived from the cosmogenic depth profile (Fig. 6). This discrepancy might reveal a complex history of sedimentation/erosion in the time since abandonment of the terrace. Several scenarios are possible, including a hiatus in loess deposition between terrace abandonment at ~88ka to ~38 ka characterized by either non-deposition of loess and/or erosion of the river. These uncertainties therefore make it difficult to constrain the true abandonment age of this particular terrace between ~88ka to ~38 ka. At BBK1 and BBK2, the thickness of loess is relatively low and the associated uncertainties are consequently lower. At these two sites, the hypothetical maximum and minimum abandonment ages (calculated by assuming either instantaneous deposition of the entire loess layer immediately after terrace abandonment, or very recent deposition of the loess, respectively) are similar (Fig. 6).

4.3 Diffusion across fault-scarps

4.3.1 Methods

We also constrained the ages of some of the terraces that were not sampled for cosmogenic analysis or IRSL dating, by quantifying the fault scarp degradation. The topographic shape of a scarp affecting a terrace surface reflects the interplay between faulting and degradation by erosion. The scarp topography therefore a function of the fault activity and dip, the age of the terrace, and surface processes (Arrowsmith et al., 1998; Avouac and Peltzer, 1993; Nash, 1980). In the absence of gullying or shallow landslide processes, downhill mass transfer across the scarps is generally assumed to occur through diffusion-like processes (i.e. the transfer is assumed to be proportional to the local topographic slope). If the diffusion coefficient that controls the mass transfer efficiency is known, then the scarp profile can be inverted in order to determine/decipher the terrace age. However, unlike terrace risers, the profile of an active tectonic scarp maintains steeper slopes around the piercing point of the

fault and by consequence maintains a more triangular (and therefore less gaussian) shape of the slope transverse profile (e.g. Avouac and Peltzer, 1993).

In order to unravel the scarp age from diffusional profiles, we built a numerical model based on incremental fault activity with surface rupturing, associated with an interseismic period during which the diffusion erosional processes degrade the refreshed scarp. We assumed that after each rupture, the overhanging part of the scarp collapses vertically onto the the footwall surface. We also assumed that any new ruptures would break the surface at the piercing point of the previous rupture. During interseismic periods, the diffusion equation is solved iteratively through a finite difference scheme. Thus, in our model, the evolution of a given reverse fault scarp depends on five parameters, including 1) the coseismic slip increment, 2) the fault dip, 3) the initial uniform slope of the terrace surface, 4) the time of its abandonment, and 5) the diffusion coefficient. The initial slope of the faulted surface can be estimated from the far field profile elevation across the fault. Based on paleoseismic evidence from active faults further west in Kyrgyzstan (Thompson et al, 2002), we considered series of 0.5 to 2.5m slips that were generated on a single fault plane dipping at $35\pm 5^\circ$. Though the total deformation rate is greater in this region, the range of slip values considered is large enough to correspond to the eastern part as well. Thus, if either the time of abandonment or the diffusion coefficient is independently known, the other can be determined by adjusting the model to the elevation data using a least square procedure. In both cases, the confidence intervals for the diffusion coefficient or the terrace age were defined by considering a mean square deviation (between the measured elevations and the modeled elevations) within 5 cm of the minimum misfit (see Fig. 4 of Avouac (1993)).

4.3.2 Calibration of the diffusion

The analysed profiles were carefully selected from field observations and satellite image analyses in order to avoid non-diffusive processes across the tectonic scarps, for example shallow landslides with partial scarp collapse, stream incision and gullyng, loess deposition, or alluvial fan deposition from a lateral stream along the scarp footwall.

In order to calibrate the diffusion coefficients, we selected five fault scarps where the ages of the affected alluvial terrace had already been determined from the cosmogenic depth profile inversion (see example in Fig. 7A and all results in Fig. D in the online depository). These included sites BBK3 and BBK4, where two faults and their associated scarps were analyzed. The calibration results are given in Table 1 and are plotted against the ages of the terraces in Figure 7B. The coefficients range from $8^{+6.6}_{-3.3}$ m²/ka to $13^{+7.8}_{-7.3}$ m²/ka with a weighted average value of 10.3 ± 1.4 m²/ka, and do not display any obvious change between the old and young terraces. However, these consistent values are higher than other estimates in the northern Tianshan (Avouac, 1993; Wei et al., 2015), a difference that might be related to variations in the local climate (for example, a colder climate in our study area).

In all cases, the whole height of the scarp was considered, including any pressure ridges present at the tops of the scarps (Fig. 7A and Fig. D). The absence of significant variations in diffusion with time or scarp elevation, as well as the low discrepancy, at least within the confidence intervals, between values calculated for the two sites, suggests that, in this particular region, the diffusion processes are relatively steady and are spatially uniform. Even though the analysis above is based on only five profiles, and thus more scarps would need to be included to obtain a higher statistical relevance, we consider these preliminary results to be sufficiently robust to be used for dating other fault scarps.

4.3.3 Dating fault-scarps and sensitivity of the age inversion

The elevation profiles were inverted to date the scarps in the western part of the Bayanbulak basin (BBK2), in the central part of the basin at site BBK3 across fault F5 (terrace T4) and at BBK4 across fault F3 (terrace T1), in the eastern part of the basin (BBK5), and finally in the Nalati basin (site Narat1). The results of the profile inversion are presented in Figure 7 and the ages derived from this analysis are given in Table 1.

As the morphological dating was based on a series of model assumptions and parameters, we tested the sensitivity of the model by modifying several of these assumptions: multiple instead of single points, the presence of a pressure ridge at the top of the scarp, and non-linear diffusion processes when slopes approach the stability angle of repose (Fig. E). In all of the cases tested, these complexities did not significantly affect our scarp age estimates and in each case, ages were overestimated by no more than 20% (see online depository). The derived slip rates must therefore be considered as minimum values. For the Nalati scarp, the ~1.4 Ma age is much older than in the Bayanbulak basin. On such a time scale, we cannot exclude any changes in diffusion efficiency, or loess deposition, that could have significantly biased our age estimates. However, even if true age would be two or three times younger than the present estimate, the shortening rate would still be limited to a relatively subdued value of ~0.1 mm/yr, a value too low to have a significant impact on the shortening budget across the inner Tianshan.

5. DENUDATION RATES FROM COSMOGENIC ANALYSES

The average denudation rate of an entire drainage basin can be estimated by measuring the mean cosmogenic nuclide concentration in a river sand at the basin outlet and estimating the average basin-wide rates of ^{10}Be production (at/g/yr) by neutrons, slow muons and fast muons (Brown et al., 1995).

The mean cosmogenic concentration was initially derived from the inherited concentrations derived from the depth profile inversion. These values may represent the

average concentrations of cosmogenic nuclides shed by the rivers at the time of terrace fill accumulation. However, the sediments deposited at site BBK1 were transported by the larger Kaidu river, which meanders through the Bayanbulak basin within a large flood plain where complex sediment recycling likely occurred. These concerns are also consistent with the higher inherited concentration measured in the BBK1-T2 depth profile (Fig. 6), which suggests a significant contribution of highly concentrated and enriched in ^{10}Be flood plain sediments. As it is difficult to correct for such contamination, we limited our analyses to sites BBK3 and BBK4, where any contamination was likely negligible due to the greater transport distance from the hills. To complement the denudation rates derived from the inherited concentrations, we also collected 3 samples of present-day sand from rivers draining the internal ranges of the Tianshan (Fig. 1C and Fig. F). These samples were treated and measured in the same way as for the depth profile samples, and the results are reported in Table A.

In all cases, denudation rates were estimated using present-day cosmogenic production rates. Because the terraces studied are relatively young (Fig. 6) we can assume that the drainage basins have not changed significantly since the accumulation of the terrace fill. However, for site BBK4, the profile was collected in a small gully that cuts the fault scarps and therefore the drainage basin at the time of terrace abandonment is undefined. The present watershed of the closest river is relatively small (11.7 km²) and it is possible that the sediments analyzed actually have originated from an alluvial fan shed from a larger catchment area located to the east, three times bigger than the present one (Fig. D). We therefore considered both of these possibilities in our calculation, though this has little impact on the absolute value of the production rate (Table 2).

The basin-scale average cosmogenic production rates were computed in ArcGIS, using an in-house plug-in which averages the local production rates of each point in the study basin. The local production rates were also calculated using a sea level high-latitude (SLHL) ^{10}Be production rate of 3.9 ± 0.1 (compiled by Balco et al. (2009) and revised by Braucher et al. (2011) to include the slow and fast muons contribution), scaled according to Stone (2000) for the local latitude and altitude derived from SRTM at 90 m resolution. We also included a correction factor for shielding by the surrounding topography in our calculations (see Table 1). The latter was computed for each individual pixel of the D.E.M. using the ArcGIS(R) tools developed by Codilean et al. (2006), which use a relief shadow modeling technique to identify the area of obstructed radiation.

Finally, in order to estimate the uncertainties in the denudation rates, we propagated errors in the cosmogenic production rates and the measured concentrations by assigning an uncertainty of 9 % to the spallogenic production parameters (Balco et al., 2009) and a conservative value of 50 % for both types of muons. The results are reported in Table 2 along with the cosmogenic production rates and correcting topographic factors. In the central Tianshan, our denudation rate estimates range from 0.08 to 0.27 mm/yr (Table 2) with an average of 0.14 ± 0.1 mm/yr. The two paleo-denudation rates at 22 ka (BBK3) and 64 ka (BBK4) are similar to the present-day rates, suggesting no changes in denudation during the late Pleistocene.

5. DISCUSSION

5.1 Shortening rates and the distribution of deformation

Using our estimates of the amount of shortening and the terrace abandonment ages, we calculated the shortening rates at each study site (Table1). Over the last ~100 kyr, the total crustal shortening across the Narat range between the Bayanbulak and the Nalati basins reaches 1.36 ± 0.70 mm/yr, suggesting that the shortening accommodated across this internal range represents a significant fraction (possibly at least ~15 %) of the total ~8.5 mm/yr crustal shortening across the entire Tianshan. While our crustal shortening rates should be treated with some degree of caution because of the large uncertainties in the fault dip angles, they would nevertheless remain significant (>0.5 mm/yr) even if the angles of the faults were steeper (60°). Moreover, it is likely that active deformation exists on the southern side of the Yili basin as well (Fig. 5), though the detection of potentially active faults from field observations or satellite images remains difficult here due to the high and rugged topography in this part of the range. The 700 km long Bolokenu-Aqikekuduk (Bo-A) and Kashi river fault zones present additional evidence for Late Quaternary deformation and also experienced strong earthquake activity in the recent past ($M=7.4$ in 1944 and $M=8$ in 1812) (Fang et al., 2014; Shen et al., 2011). These observations support our conclusion that a significant fraction of the active deformation is accommodated within the central part of the Eastern Tianshan.

In the Western Tianshan, GPS velocity measurements (Yang et al., 2008) indicate that 55 % of the present-day crustal shortening across the range (~20 mm/yr) is distributed along the North and South piedmonts and that 45 % is distributed within the central part of the range (9 mm/yr, Thompson et al., 2002). In the easternmost Tianshan, the distribution of deformation across the range remains unknown but evidence for crustal shortening is also found within the central part where ~1 mm/yr of shortening is accommodated in the Turfan and Yanqi basins (Shen et al., 2011; Huang et al., 2014). Therefore, our the results of our study, together with previous findings, suggest that 15 to 45 % of the total shortening across the range is accommodated by the inner structures.

5.3 Growth of the Tianshan range: crustal thickening vs. denudation rates

Along the transect studied, the eastern Tianshan is around ~270 km wide and the average thickness of the crust on either side of the range is estimated to be ~50 km (Cotton and Avouac, 1994; Poupinet et al., 2002). In assuming a simple 2D conservation mass across the wide range, and also assuming that the width of the range is constant or increases at a negligible rate, a total shortening rate between the Tarim and the Junggar basins of 8.5 ± 0.5 mm/yr (Yang et al., 2008) would lead to an average crustal thickening rate of about 1.6 mm/yr. It is interesting to compare this value with the rate of erosion at the scale of the entire range. Along the northern and southern Tianshan piedmonts, the average denudation rates derived from cosmogenic analyses in foreland sediments or mass balance in alluvial fans ranged from 0.1 to 0.6 mm/yr during the Late Pleistocene (Charreau et al., 2011; Guerit et al., 2016; Puchol et al., 2016). Therefore, at the scale of the whole range the crustal thickening significantly outpaces the denudation. In the central part of the range, based on the ~1.4 mm/yr of shortening accommodated across the Narat range and assuming pure shear deformation distributed over a width of ~50 km (from the center of the Bayanbulak basin to

the center of the Nalati basin) and uniformly down to the moho (~50km), we obtain a broadly similar crustal thickening rate of ~1.4 mm/yr across this particular range. This value is ten times greater than the average denudation rate of 0.14 mm/yr that we found in the central part. Therefore, the crustal thickening rate in the Eastern Tianshan is significantly greater than the average denudation rates, at both the regional scale and at the scale of the central part of the range. This disequilibrium is likely due to the arid climate in the region, which possibly limits the denudation (Guerit et al., 2016). The topography of the range has therefore not yet reached steady-state topography: in addition to probable lateral growth by outward propagation of deformation along the southern and northern piedmonts, the range continues to grow mostly by activating internal deformation. Given the difference between the average thickening rates and the average denudation rates, the net growth rate of crustal thickness would therefore be ~1.25 mm/yr, and the mean surface of central Tian Shan would gain 0.2 mm per year or 200 m per Myr.

The calculated thickening rate across the whole transect of eastern Tianshan range is similar to that calculated across the internal Narat range. This might suggest homogeneous shortening and thickening at the scale of the range. However, to confirm this hypothesis, a complete description of the fault activity across the range, and more importantly a good understanding of the thickening process in the middle and lower crust, by overthrusting, underplating, or viscous flow, would be required. Nevertheless, we note that at the surface, deformation of the inner range seems to preferentially occur along inherited Paleozoic structures and crustal weakness zones that were reactivated during the Cenozoic Indo-Asian orogeny (Dumitru et al., 2001; Jolivet et al., 2010; Poupinet et al., 2002). These structures probably focused the deformation along a number of separated active zones, resulting in the presence of large undeformed areas inbetween these zones (Dumitru et al., 2001; Jolivet et al., 2010). In the case of such strong structural inheritance, the long term crustal shortening of the

range could lead to the closure of all intermontane basins in the Tianshan, gradually leading to a state of dynamic equilibrium and steady-state topography. As suggested by a mean surface uplift rate of 200m/Myr, the time needed to reach this equilibrium might be very long due to the very low denudation in this arid region (J.-P. Avouac and Burov, 1996). However, since the Tianshan range is already relatively high and large, it might never reach the final double-vergent wedge shaped morphology, but may instead evolve toward an orogenic plateau due to the thermomechanical strength limit of thickened crust (e.g. Vanderhaeghe et al., 2003).

6. CONCLUSION

Our results indicate that in the central eastern part of the Tianshan range the crustal thickening outpaces denudation. This is also likely true at the scale of the whole Tianshan. More systematic estimates of the denudation rates across the range, as well as estimates of the slip rates on several unstudied thrusts, are now required to more precisely estimate the balance between thickening rate and denudation. Moreover, our thickening rates remain first order estimates based on simple 2D conservation mass and simple shear across the range. More accurate calculations in the future should consider sediment recycling and erosion within the piedmont as well as enlargement rate of the range. Nevertheless, the Tianshan appears to represent a reference case of a range experiencing distributed deformation induced by inherited crustal heterogeneities and non-steady-state topographic growth, possibly because of low denudation in this arid region.

ACKNOWLEDGMENTS

This study was financed by the French INSU/CNRS SYSTER program. This is CRPG contribution n° XXXX.

BIBLIOGRAPHY

- Arrowsmith, J.R., Rhodes, D.D., Pollard, D.D., 1998. Morphologic dating of scarps formed by repeated slip events along the San Andreas Fault, Carrizo Plain, California. *J. Geophys. Res.* 103, 10141–10160.
- Avouac, J., Burov, E.B., 1996. Erosion as a driving mechanism of intracontinental mountain growth. *J. Geophys. Res.* 101, 17747–17769.
- Avouac, J.-P., 1993. Analysis of scarp profiles: Evaluation of errors in morphologic dating. *J. Geophys. Res.* 98, 6745. doi:10.1029/92JB01962
- Avouac, J.-P., Burov, E.B., 1996. Erosion as a driving mechanism of intracontinental mountain growth. *J. Geophys. Res.* 101, 17747.
- Avouac, J.P., Peltzer, G., 1993. Active tectonics in southern Xinjiang, China: analysis of terrace riser and normal fault scarp degradation along the Hotan-Qira fault system. *J. Geophysical Res.* 98, 21773–21807.
- Balco, G., Briner, J., Finkel, R.C., Rayburn, J.A., Ridge, J.C., Schaefer, J.M., 2009. Regional beryllium-10 production rate calibration for late-glacial northeastern North America. *Quat. Geochronol.* 4, 93–107. doi:10.1016/j.quageo.2008.09.001
- Braucher, R., Bourlès, D.L., Brown, E.T., Colin, F., Muller, J.-P., Braun, J.-J., Delaune, M., Minko, A.E., Lescouet, C., Raisbeck, G.M., Yiou, F., 2000. Application of in situ-produced cosmogenic ^{10}Be and ^{26}Al to the study of lateritic soil development in tropical forest: theory and examples from Cameroon and Gabon. *Chem. Geol.* 170, 95–111.
- Braucher, R., Del Castillo, P., Siame, L., Hidy, A.J., Bourlès, D.L., 2009. Determination of both exposure time and denudation rate from an in situ-produced ^{10}Be depth profile: A mathematical proof of uniqueness. Model sensitivity and applications to natural cases. *Quat. Geochronol.* 4, 56–67. doi:10.1016/j.quageo.2008.06.001

541 Braucher, R., Merchel, S., Borgomano, J., Bourlès, D.L., 2011. Production of cosmogenic
 542 radionuclides at great depth: A multi element approach. *Earth Planet. Sci. Lett.*
 543 doi:10.1016/j.epsl.2011.06.036
 544 Brown, E.T., Stallard, R.F., Larsen, M.C., Raisbeck, G.M., Yiou, F., 1995. Denudation rates
 545 determined from the accumulation of in situ produced ^{10}Be in the Luquillo experimental
 546 forest, Puerto-Rico. *Earth Planet. Sci. Lett.* 129, 193–202.
 547 Charreau, J., Blard, P.H., Puchol, N., Avouac, J.P., Lallier-Vergès, E., Bourlès, D., Braucher,
 548 R., Gallaud, A., Finkel, R., Jolivet, M., Chen, Y., Roy, P., 2011. Paleo-erosion rates in
 549 Central Asia since 9Ma: A transient increase at the onset of Quaternary glaciations?
 550 *Earth Planet. Sci. Lett.* 304, 85–92. doi:10.1016/j.epsl.2011.01.018
 551 Charvet, J., Shu, L.S., Laurent-Charvet, S., 2007. Paleozoic structural and geodynamic
 552 evolution of eastern Tianshan (NW China): welding of the Tarim and Junggar plates.
 553 *Episodes* 30, 162–186.
 554 Chmeleff, J., von Blanckenburg, F., Kossert, K., Jakob, D., 2010. Determination of the ^{10}Be
 555 half-life by multicollector ICP-MS and liquid scintillation counting. *Nucl. Instruments*
 556 *Methods Phys. Res. Sect. B Beam Interact. with Mater. Atoms* 268, 192–199.
 557 Codilean, A.T., 2006. Calculation of the cosmogenic nuclide production topographic
 558 shielding scaling factor for large areas using DEMs. *Earth Surf. Process. Landforms* 31,
 559 785–794.
 560 Cotton, F., Avouac, J.P., 1994. Crustal and upper-mantle structure under the Tien Shan from
 561 surface-wave dispersion. *Phys. Earth Planet. Inter.* 84, 95–109. doi:10.1016/0031-
 562 9201(94)90036-1
 563 Dahlen, F.A., Suppe, J., 1988. Mechanics, growth, and erosion of mountain belts, in: Clark,
 564 S.P., Burchfiel, B.C., Suppe, J. (Eds.), *Processes in Continental Lithospheric*
 565 *Deformation*. Geological Society of America Special Paper, pp. 161–178.

566 Dumitru, T. a, Zhou, D., Chang, E.Z., Graham, S. a, Hendrix, M.S., Sobel, E.R., Carroll,
 567 A.R., 2001. Uplift, exhumation, and deformation in the Chinese Tian Shan. *Mem. - Geol.*
 568 *Soc. Am.* 194, 71–99. doi:10.1130/0-8137-1194-0.71
 569 Fang, L., Wu, J., Wang, C., Wang, W., Yang, T., 2014. Relocation of the 2012 M s6.6
 570 Xinjiang Xinyuan earthquake sequence. *Sci. China Earth Sci.* 57, 216–220.
 571 doi:10.1007/s11430-013-4755-6
 572 Gosse, J.C., Phillips, F.M., 2001. Terrestrial in situ cosmogenic nuclides: theory and
 573 application. *Quat. Sci. Rev.* 20, 1475–1560.
 574 Guerit, L., Barrier, L., Jolivet, M., Fu, B., Métivier, F., 2016. Denudation intensity and control
 575 in the Chinese Tian Shan : new constraints from mass balance on catchment-alluvial fan
 576 systems 1106, 1088–1106. doi:10.1002/esp.3890
 577 Guralnik, B., Matmon, A., Avni, Y., Porat, N., Fink, D., 2011. Constraining the evolution of
 578 river terraces with integrated OSL and cosmogenic nuclide data. *Quat. Geochronol.* 6,
 579 22–32. doi:10.1016/j.quageo.2010.06.002
 580 Hancock, G.S., Anderson, R.S., Chadwick, O.A., Finkel, R.C., 1999. Dating fluvial terraces
 581 with ¹⁰Be and ²⁶Al profiles: application to the Wind River, Wyoming. *Geomorphology*
 582 27, 41–60.
 583 Jolivet, M., Dominguez, S., Charreau, J., Chen, Y., Li, Y., Wang, Q., 2010. Mesozoic and
 584 Cenozoic tectonic history of the central Chinese Tian Shan: Reactivated tectonic
 585 structures and active deformation. *Tectonics* 29, 1–30. doi:10.1029/2010TC002712
 586 Korschinek, G., Bergmaier, A., Faestermann, T., Gerstmann, U.C., Knie Rugel, G., K.,
 587 Wallner, A., Dillmann, I., Dollinger, G., Lierse von Gosstonski, C., Kossert, K., Maiti,
 588 M., Poutivtsev, M., Remmert, A., 2010. A new value for the ¹⁰Be half-life by Heavy-Ion
 589 Elastic Recoil detection and liquid scintillation counting. . *Nucl. Inst. Meth. B* 268, 187–
 590 191.

591 Lal, D., 1991. Cosmic ray labeling of erosion surfaces: in situ nuclide production rates and
 592 erosion models. *Earth Planet. Sci. Lett.* 104, 424–439.

593 Long, H., Shen, J., Tsukamoto, S., Chen, J., Yang, L., Frechen, M., 2014. Dry early Holocene
 594 revealed by sand dune accumulation chronology in Bayanbulak Basin (Xinjiang, NW
 595 China). *The Holocene* 24.

596 Nash, D.B., 1980. Morphological analysis of degraded normal fault scarps. *J. Geol.* 88, 353–
 597 360.

598 Poupinet, G., Avouac, J.-P., Jiang, M., Wei, S., Kissling, E., Herquel, G., Guilbert, J., Paul,
 599 A., Wittlinger, G., Su, H., Thomas, J.-C., 2002. Intracontinental subduction and
 600 palaeozoic inheritance of the lithosphere suggested by a teleseismic experiment across
 601 the Chinese Tien Shan. *Terra Nov.* 14, 18–24.

602 Puchol, N., Charreau, J., Blard, P., Lavé, J., Dominguez, S., Pik, R., Saint-carlier, D., ASTER
 603 Team, 2016. Limited impact of Quaternary glaciations on denudation rates in central
 604 Asia. *Geol. Soc. Am. Bull.*

605 Reigber, C., Michel, G.W., Galas, R., Angermann, D., Klotz, J., Chen, J.Y., Papschev, A.,
 606 Arslanov, R., Tzurkov, Ishanov, M.C., V.E., 2001. New space geodetic constraints on
 607 the distribution of deformation in the Central Asia. *Earth Planet. Sci. Lett.* 191, 157–165.

608 Saint-Carlier, D., Charreau, J., Lavé, J., Blard, P.H., Dominguez, S., Avouac, J.P., Wang, S.,
 609 Arnold, M., Aumaître, G., Keddadouche, K., Léanni, L., Chauvet, F., Bourlés, D.L.,
 610 2016. Major temporal variations in shortening rate absorbed along a large active fold of
 611 the southeastern Tianshan piedmont (China). *Earth Planet. Sci. Lett.* 434, 333–348.
 612 doi:10.1016/j.epsl.2015.11.041

613 Shen, J., Wang, Y., Li, Y., 2011. Characteristics of the Late Quaternary right-lateral strike-
 614 slip movement of Bolokenu-Aqikekuduk fault in northern Tianshan Mountains, NW
 615 China. *Geosci. Front.* 2, 519–527. doi:10.1016/j.gsf.2011.05.004

616 Song, Y., Li, C., Zhao, J., Cheng, P., Zeng, M., 2012. A combined luminescence and
617 radiocarbon dating study of the Ili loess, Central Asia. *Quat. Geochronol.* 2–7.

618 Stone, J.O., 2000. Air pressure and cosmogenic isotope production. *J. Geophys. Res. - Solid*
619 *Earth* 105, 23753–23759.

620 Tapponnier, P., Molnar, P., 1979. Active faulting and cenozoic tectonics of the Tien Shan,
621 Mongolia, and Baykal regions. *J. Geophys. Res.* 84, 3425–3459.

622 Thiel, C., Buylaert, J., Murray, A., Terhorst, B., Hofer, I., Tsukamoto, S., Frechen, M., 2011.
623 Luminescence dating of the Stratzing loess profile (Austria) and Testing the potential of
624 an elevated temperature post-IR IRSL protocol. *Quat. Int.* 234, 23–31.
625 doi:10.1016/j.quaint.2010.05.018

626 Thompson, S.C., Weldon, R.J., Rubin, C.M., Abdrakhmatov, K., Molnar, P., Berger, G.W.,
627 2002. Late Quaternary slip rates across the central Tien Shan, Kyrgyzstan, central Asia
628 107. doi:10.1029/2001JB000596

629 Uppala, S.M., Kållberg, P.W., Simmons, A.J., Andrae, U., Bechtold, V.D.C., Fiorino, M.,
630 Gibson, J.K., Haseler, J., Hernandez, A., Kelly, G.A., Li, X., Onogi, K., Saarinen, S.,
631 Sokka, N., Allan, R.P., Andersson, E., Arpe, K., Balmaseda, M.A., Beljaars, A.C.M.,
632 Berg, L. Van De, Bidlot, J., Bormann, N., Caires, S., Chevallier, F., Dethof, A.,
633 Dragosavac, M., Fisher, M., Fuentes, M., Hagemann, S., Hólm, E., Hoskins, B.J.,
634 Isaksen, I., Janssen, P.A.E.M., Jenne, R., McNally, A.P., Mahfouf, J.-F., Morcrette, J.-J.,
635 Rayner, N.A., Saunders, R.W., Simon, P., Sterl, A., Trenberth, K.E., Untch, A.,
636 Vasiljevic, D., Viterbo, P., Woollen, J., 2005. The ERA-40 re-analysis. *Q. J. R.*
637 *Meteorol. Soc.* 131, 2961–3012. doi:10.1256/qj.04.176

638 Vanderhaeghe, O., Medvedev, S., Fullsack, P., Beaumont, C., Jamieson, R. a., 2003.
639 Evolution of orogenic wedges and continental plateaux: insights from crustal thermal-
640 mechanical models overlying subducting mantle lithosphere. *Geophys. J. Int.* 153, 27–

51. doi:10.1046/j.1365-246X.2003.01861.x

- Wei, Z., Arrowsmith, J.R., He, H., 2015. Evaluating fluvial terrace riser degradation using LiDAR-derived topography: An example from the northern Tian Shan, China. *J. Asian Earth Sci.* 105, 430–442. doi:10.1016/j.jseaes.2015.02.016
- Willett, S.D., Slingerland, R., Hovius, N., 2001. Uplift, shortening, and steady state topography in active mountain belts. *Am. J. Sci.* 301, 455–485.
- Wu, C., Wu, G., Shen, J., Chen, J., Alimujiang, Chang, X., 2014. The Late Quaternary activity of the Nalati Fault and its implication for the crustal deformation in the interior of the Tianshan mountains. *Igarss 2014* 1–5. doi:10.1007/s13398-014-0173-7.2
- Yang, Q., Cui, C., 2005. Impact of climate change on the surface water of Kaidu River Basin. *J. Geogr. Sci.* 15, 20–28.
- Yang, S., Jie, L.I., Qi, W., 2008. The deformation pattern and fault rate in the Tianshan Mountains inferred from GPS observations 51. doi:10.1007/s11430-008-0090-8
- Yi, C.E., Lai, Z.P., Sun, Y.J., Hou, G.L., Yu, L.P., Wu, C.Y., 2012. A luminescence dating study of loess deposits from the Yili River basin in western China. *Quat. Geochronol.* 10, 50–55. doi:10.1016/j.quageo.2012.04.022

Figure captions:

Figure 1: A: structural map of the eastern Tianshan (GPS velocities relative to stable Eurasia from Yang et al., 2008). B: interpretative cross section. C: Geological map of the Bayanbulak basin. In Figure 1c, the labels 1, 2, 3, 4 and N refer to the study site and to Figures 2A, 2B, 3A, 3B, 4 and 6 in the main text, respectively. D: Interpretative cross section of the Bayanbulak basin. E: Topographic slope attitudes across the eastern Tianshan. Elevation data were extracted from the 1 arc second SRTM dataset, along a N10°E 10 km stacked profile crossing the Bayanbulak and eastern termination of the Yili basin.

Figure 2: satellite images of sites BBK1 (A) and BBK2 (B) and DGPS elevation profile on both sites projected onto a line perpendicular to the fault scarps (C). In BBK1 the elevations are given relative to the Kaidu river. The star and the colored lines indicate the location of the cosmogenic depth measurement and the topographic profiles, respectively.

Figure 3: A: Satellite image of site BBK3 (Fig.1C for location). B: DGPS elevations relative to the river that formed the alluvial surfaces at site BBK3 (projected onto a line perpendicular to the fault scarps). C: Field photograph of the western river bank at site BBK3 showing the different terrace levels. D: Satellite image of site BBK4 (see Fig.1C for location). E: B: DGPS relative elevations to the river of the alluvial surfaces in site BBK4 (projected onto a line perpendicular to the fault scarps). The stars and the colored lines indicate the location of the cosmogenic depth measurement and the topographic profiles, respectively.

Figure 4: Satellite image of the tributary valley located in the eastern part of the Bayanbulak basin, where alluvial deposits are offset by fault F6. The enlargement shows the site studied (BBK5) and the location of the DGPS profile (not corrected from the regional slope) shown in the inset diagram above. The red line indicates the locations of the topographic profiles.

Figure 5: A: Topographic map of the Nalati and Yili basins (see box 6 in Fig 1C). The black arrows indicate active tectonic scarps associated with south dipping reverse active faults. The white line shows the location of a 4 km long stacked topographic profile. B: Panorama and DGPS profile of a cumulated fault scar within the Nalati basin that has been uplifted by 60 m (see location in figure DA). C: 4 km long stacked topographic profile across the Nalati and Yili basin. D: Panorama of the southern border of the Nalati basin and Narat Range, displaying active fault scarps.

Figure 6: ^{10}Be cosmogenic concentrations as a function of depth for each of the four sites analyzed. Note that all of the fine sediments (silt, loess, soil) were considered to have a bulk density of $1.6\pm 0.2 \text{ g/cm}^3$ and that their real thicknesses were converted to a theoretical thickness corresponding to the densities of the respective terraces. The inset diagrams show the misfit plots for both the age and inheritance values.

Figure 7: Diffusion analyses of the fault scarps. A: Calibration of the diffusion coefficient across fault F3 at site BBK3. The diagram shows the changes in elevation measured across the studied fault scarps using DGPS (black crosses). The blue dashed line shows the best fit model determined using the least squares procedure. The inset diagram to the right provides the misfit variations (calculated difference between the modeled topographic profiles and the observed elevations) against the diffusion coefficient k . The inset diagram to the right compares the observed slope (filled circles) to the best-fit modeled slope (in blue) across the scarps. B: Diffusion coefficient k against the ages of the uplifted terraces. C to G: Topographic profile inversions used to date the scarps.

Figure 8: Geological cross sections and balance between crustal thickening and denudation across the entire Tianshan and Narat ranges.

Tables

Table 1: Age, uplift and shortening rates for each of the deformed surfaces dated in the study.

Table 2: Denudation rate data, including the basin average cosmogenic production rates and topographic factors, the inherited concentrations of ^{10}Be derived from the cosmogenic depth profiles, and the calculated denudation rates.

724
725

Table 1

| Offset terrace/DGPS profile | Cosmogenic or IRSL age | Uplift | K | Diffusion age | Uplift rate | Slip | Horizontal shortening | Slip rate | Horizontal shortening rate |
|---|---------------------------|--------|----------------------|---------------|-------------|-------|--------------------------|------------------|-------------------------------|
| | (ka) | (m) | (m ² /ka) | (ka) | (mm/yr) | (m) | (m) | (mm/yr) | (mm/yr) |
| BBK1 Fault 1 | | | | | | | | | |
| T2 | 88±6/7 | 9.5±1 | n.a | | 0.11±0.02 | 17±5 | 14±5 | 0.19±0.06 | 0.15±0.06 |
| T2 _(IRSL) | 39±5 | | n.a | | 0.24±0.05 | | 14±5 | <u>0.42±0.14</u> | <u>0.35±0.15</u> |
| | | | | | | | mean: | 0.31±0.1 | 0.25±0.1 |
| BBK2 Fault 2 | | | | | | | | | |
| Profile west | | 11±2 | | 158±30/80 | 0.07±0.04 | 19±6 | 16±6 | 0.12±0.07 | 0.1±0.06 |
| Profile east | | 7±1 | | 84±30/50 | 0.08±0.05 | 12±4 | 10±4 | <u>0.15±0.1</u> | <u>0.12±0.09</u> |
| | | | | | | | mean: | 0.13±0.08 | 0.11±0.07 |
| BBK3 Fault 3 (south) | | | | | | | | | |
| T2 | 22±2 | 3±0 | 8±3.3/6.6 | | 0.14±0.02 | 5±2 | 4±2 | 0.24±0.07 | 0.19±0.08 |
| T3 | 91±9/11 | 17±3 | 12±3.6/7.5 | | 0.19±0.04 | 30±9 | 24±10 | <u>0.33±0.1</u> | <u>0.27±0.11</u> |
| | | | | | | | mean: | 0.28±0.09 | 0.23±0.1 |
| BBK3 Fault 4 (center) & Fault 5 (north) | | | | | | | | | |
| T2 | 22±2 | 6±1 | 13±7.3/7.8 | | 0.27±0.05 | 10±3 | 9±3 | 0.48±0.14 | 0.39±0.16 |
| T3 | 91±9/11 | 18±3 | 12±3.8/4.9 | | 0.2±0.04 | 31±9 | 26±10 | <u>0.34±0.11</u> | <u>0.28±0.12</u> |
| | | | | | | | mean: | 0.41±0.13 | 0.34±0.14 |
| BBK3 Fault 5 | | | | | | | | | |
| T4 | | 25±4 | | 103±54/61*** | 0.25±0.14 | 44±11 | 36±14 | 0.42±0.25* | 0.35±0.23* |
| BBK4 Fault 3 | | | | | | | | | |
| T1 | | 3.5±1 | | 13±7/6 | 0.27±0.15 | 6±2 | 5±2 | 0.47±0.29 | 0.38±0.26 |
| T2 | 64±6 | 11±2 | 9±2.2/4.2 | | 0.17±0.03 | 19±6 | 16±6 | <u>0.3±0.09</u> | <u>0.25±0.1</u> |
| | | | | | | | mean: | 0.38±0.19 | 0.31±0.18 |
| | | | | | | | mean of fault 3**: | 0.33±0.14 | 0.27±0.14 |
| BBK5 Fault 6 | | | | | | | | | |
| | | 9±1 | | 54±17/19 | 0.17±0.06 | 16±5 | 13±5 | 0.29±0.13 | 0.24±0.13 |
| Nalati basin | | | | | | | | | |
| Profile Narat1E | | 45±7 | | 1393±249/268 | 0.03±0.01 | 78±23 | 64±26 | <u>0.06±0.02</u> | <u>0.05±0.02</u> |
| Total: | | | | | | | | 1.66±0.72 | 1.36±0.71 |

*not included in the total
**includes sites BBK3 and BBK4
***inverted using local calibration of K from terraces BBK3-T2 and BBK3-T3

726
727
728
729
730
731
732
733
734
735
736
737

738
739

Table 2

| Watershed | Average Altitude (m) | Topographic factor | Production rates | | | Denudation rate (mm/yr) |
|---|-------------------------|-----------------------|---|---|---|----------------------------|
| | | | Neutrons (at g ⁻¹ y ⁻¹) | Slow muons (at g ⁻¹ y ⁻¹) | Fast muons (at g ⁻¹ y ⁻¹) | |
| Paleo-denudation from inherited concentration in terraces | | | | | | |
| BBK4 bv1 (64 ka) | 3071 | 0.998 | 37.94 | 0.03 | 0.06 | 0.12±0.01 |
| BBK4 bv2 (64 ka) | 3166 | 0.995 | 39.99 | 0.03 | 0.06 | 0.13±0.01 |
| BBK3-T2 (22ka) | 3155 | 0.996 | 39.73 | 0.03 | 0.06 | 0.13±0.01 |
| Present denudation from river bed samples | | | | | | |
| Yili | 2694 | 0.995 | 31.07 | 0.03 | 0.06 | 0.27±0.03 |
| BBK | 3155 | 0.996 | 39.73 | 0.03 | 0.06 | 0.08±0.00 |
| BBKS | 3404 | 0.992 | 45.71 | 0.04 | 0.07 | 0.12±0.01 |

740

Figure1

[Click here to download high resolution image](#)

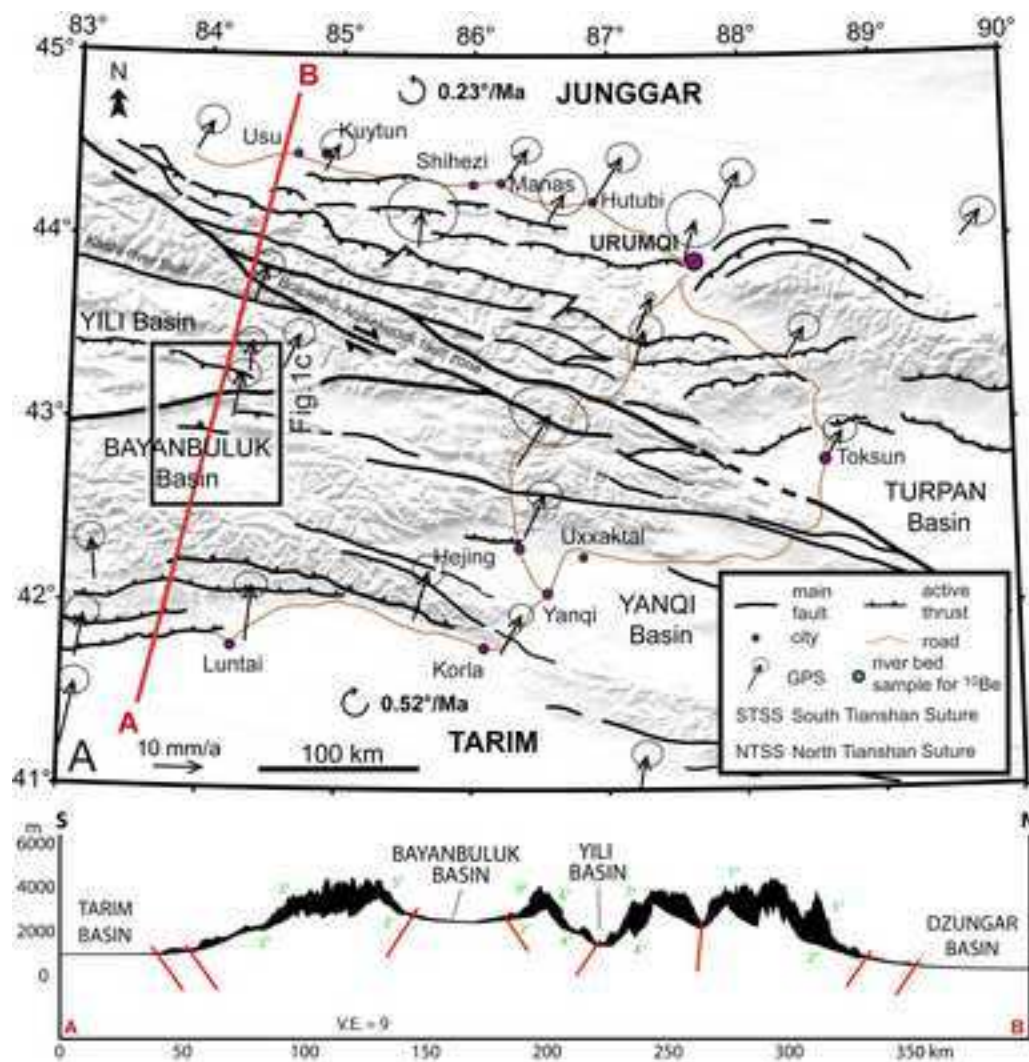


Figure 1

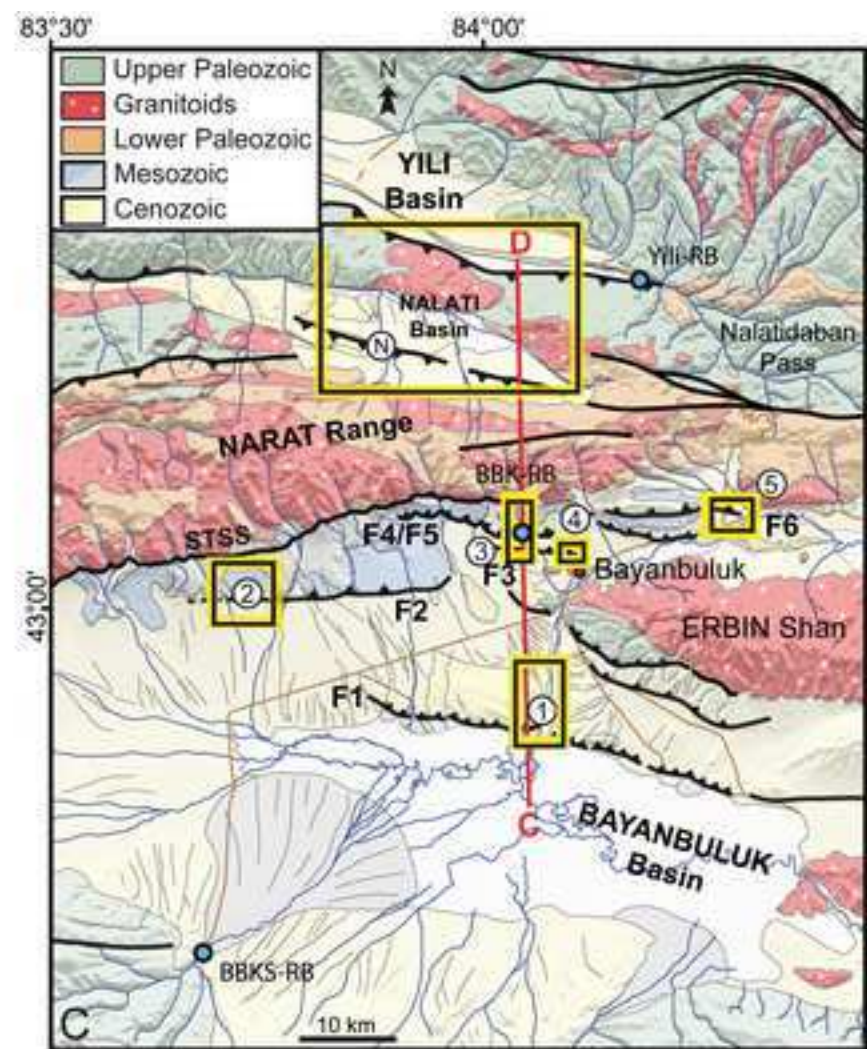


Figure 2

Figure2

[Click here to download high resolution image](#)

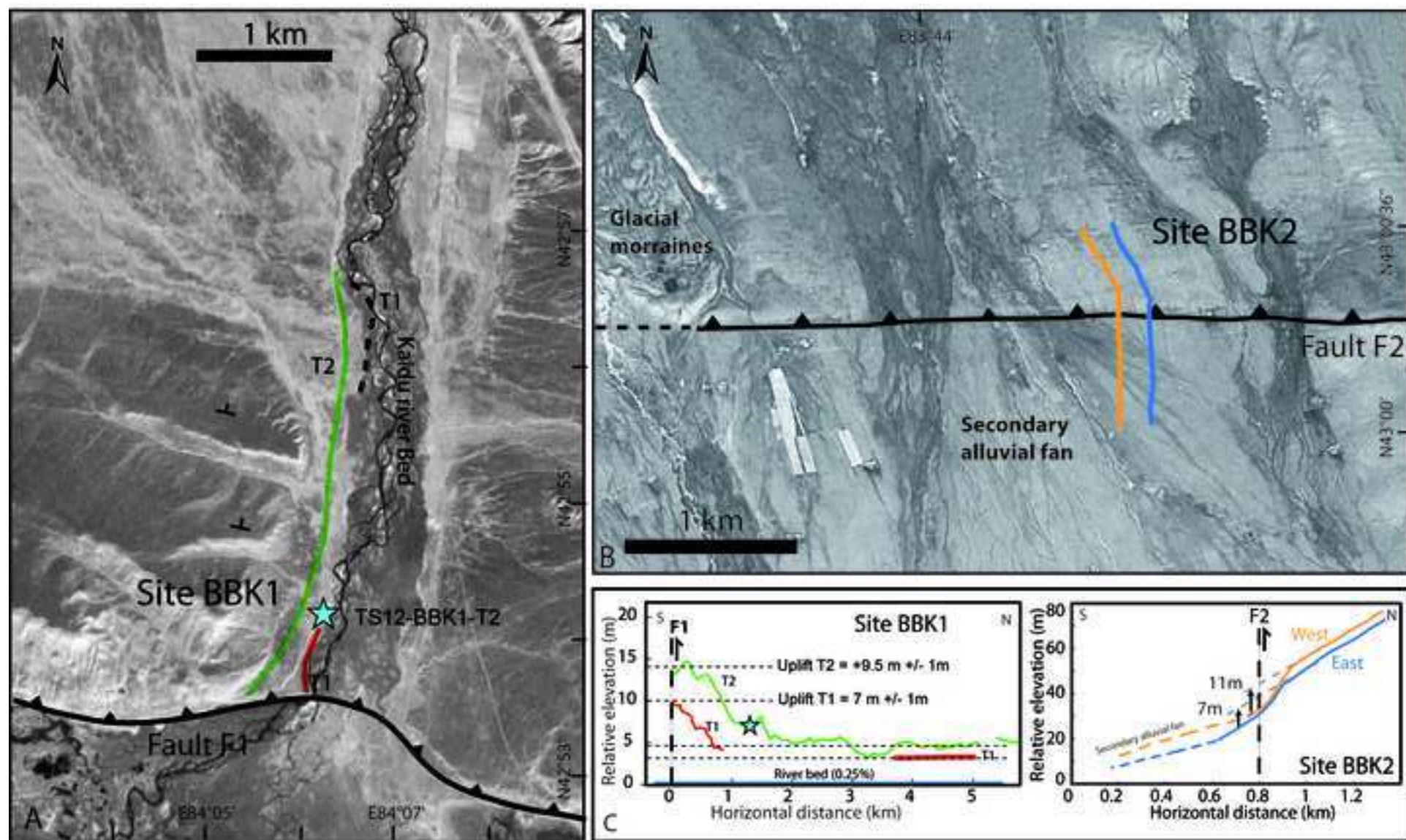


Fig. 2

Figure3
[Click here to download high resolution image](#)

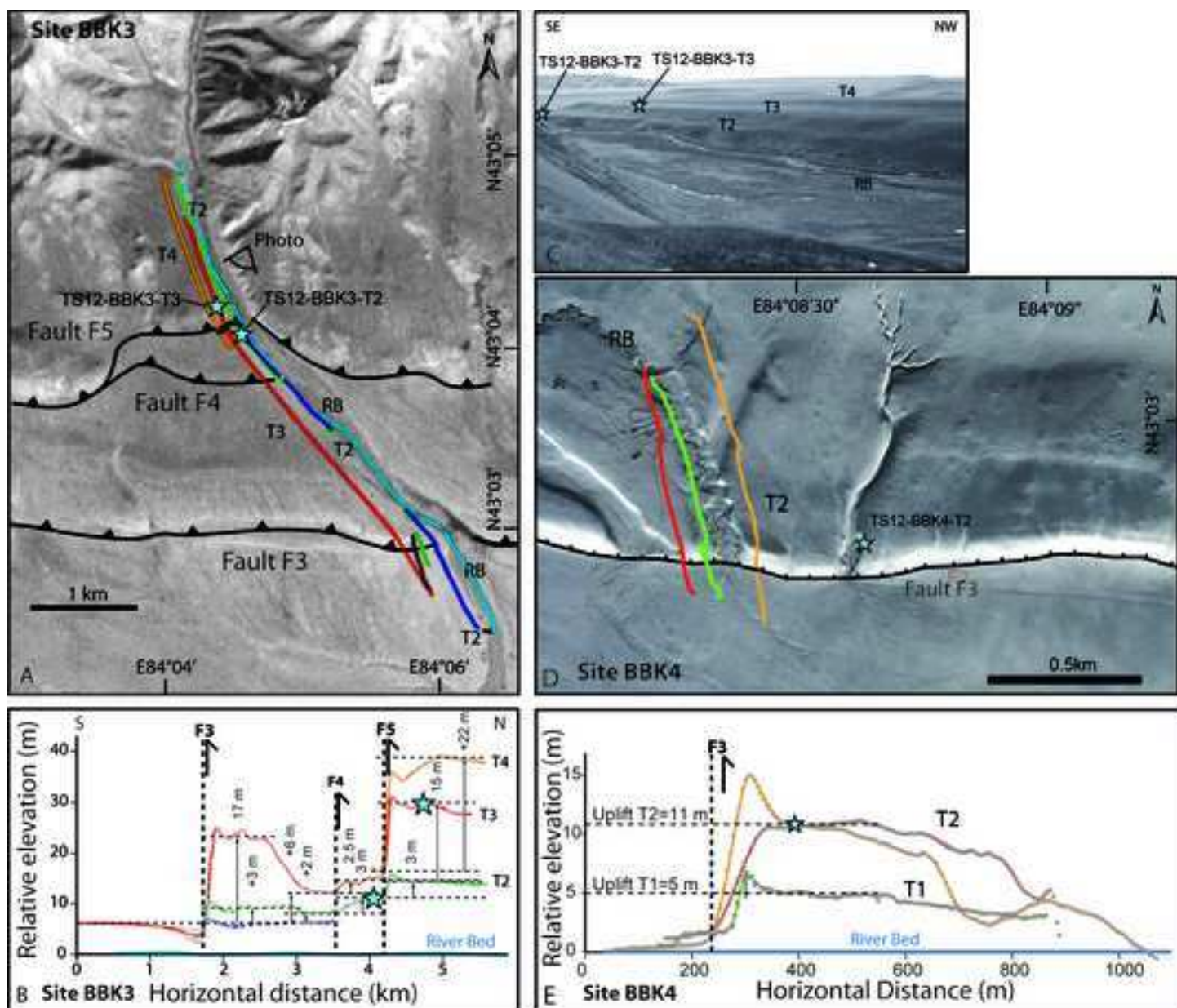


Fig. 3

Figure4

[Click here to download high resolution image](#)

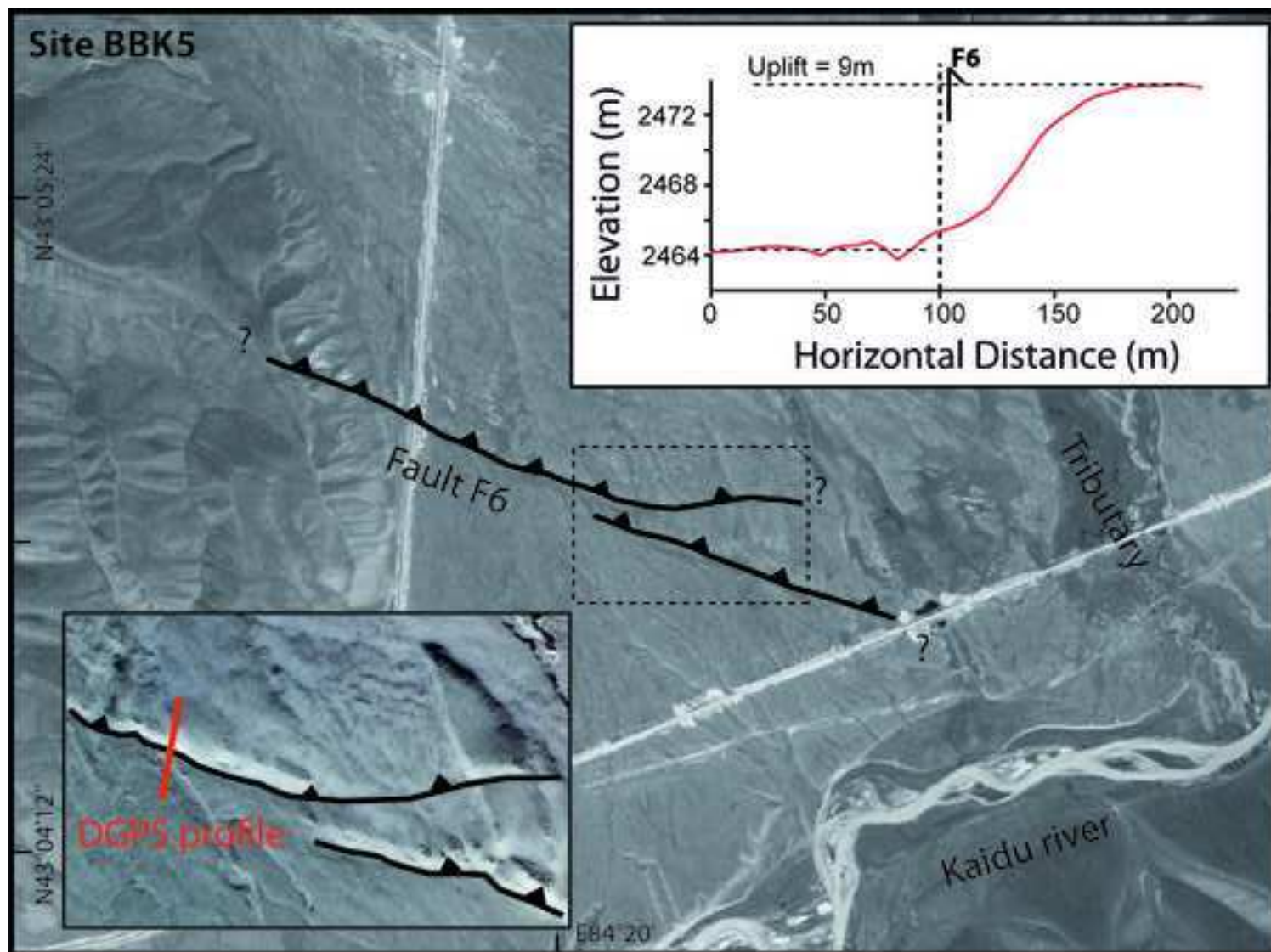


Fig. 4

Figure5
[Click here to download high resolution image](#)

Fig. 5

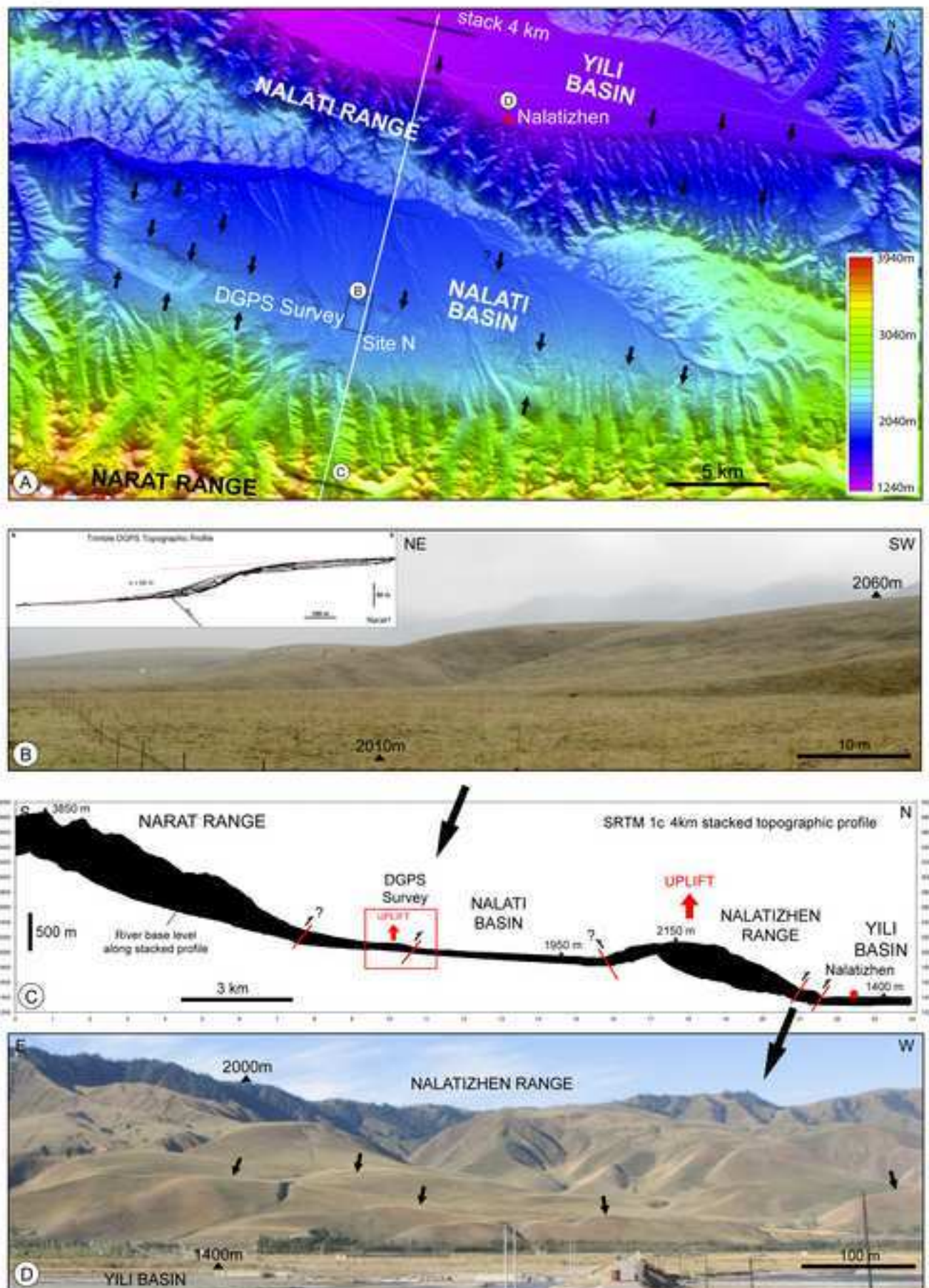


Figure6
[Click here to download high resolution image](#)

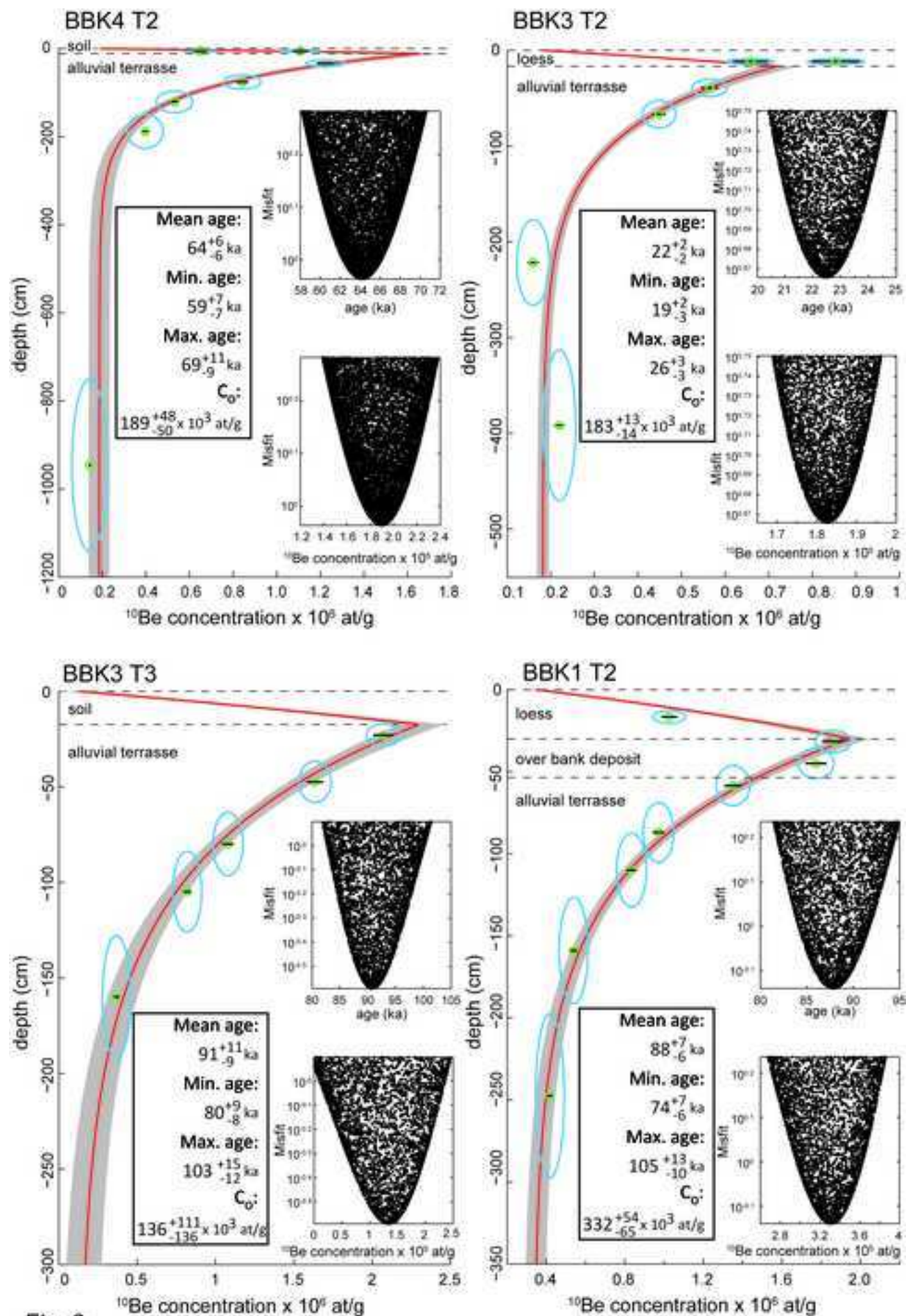


Fig. 6

Figure7
[Click here to download high resolution image](#)

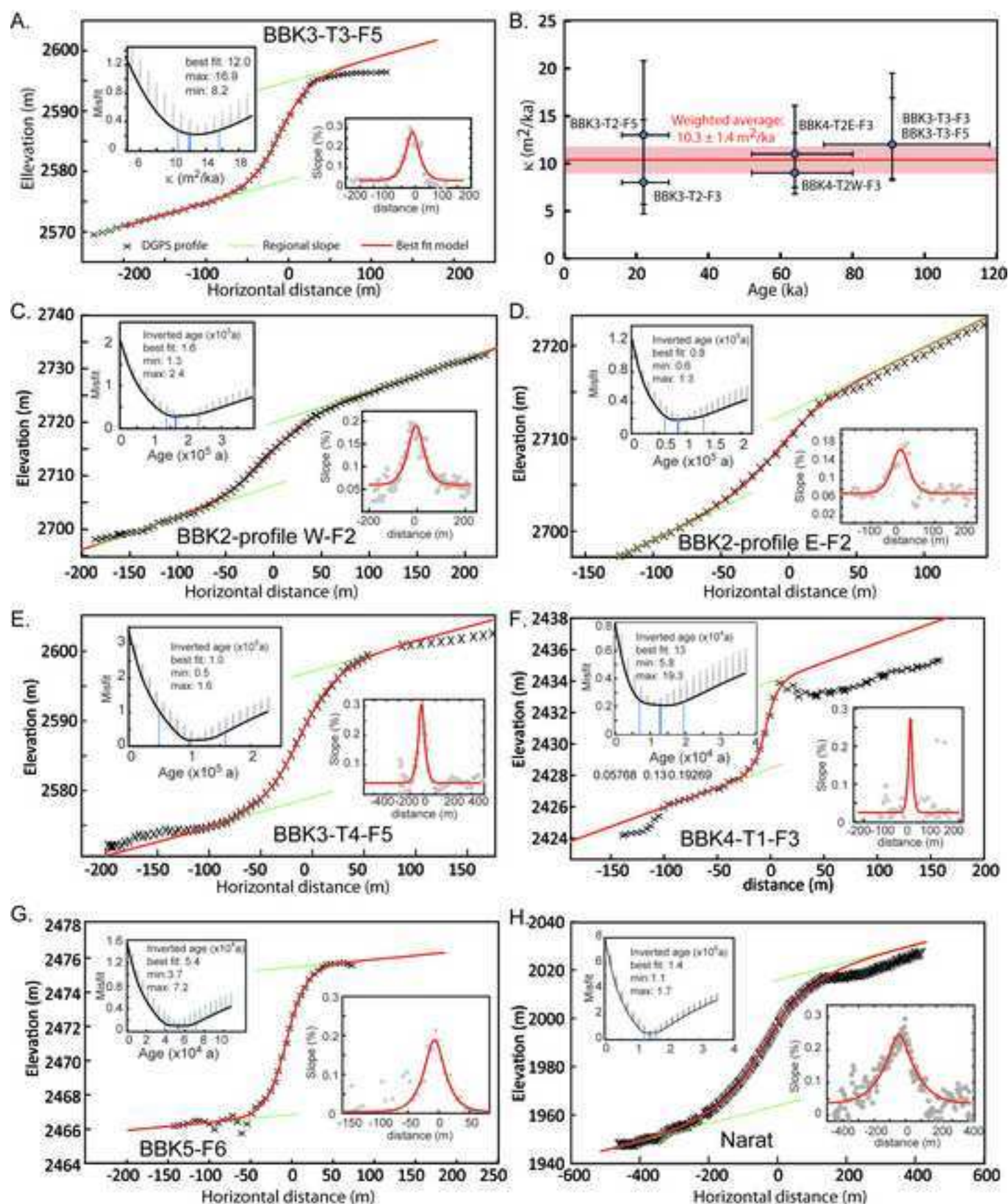


Fig. 7

Figure8

[Click here to download high resolution image](#)

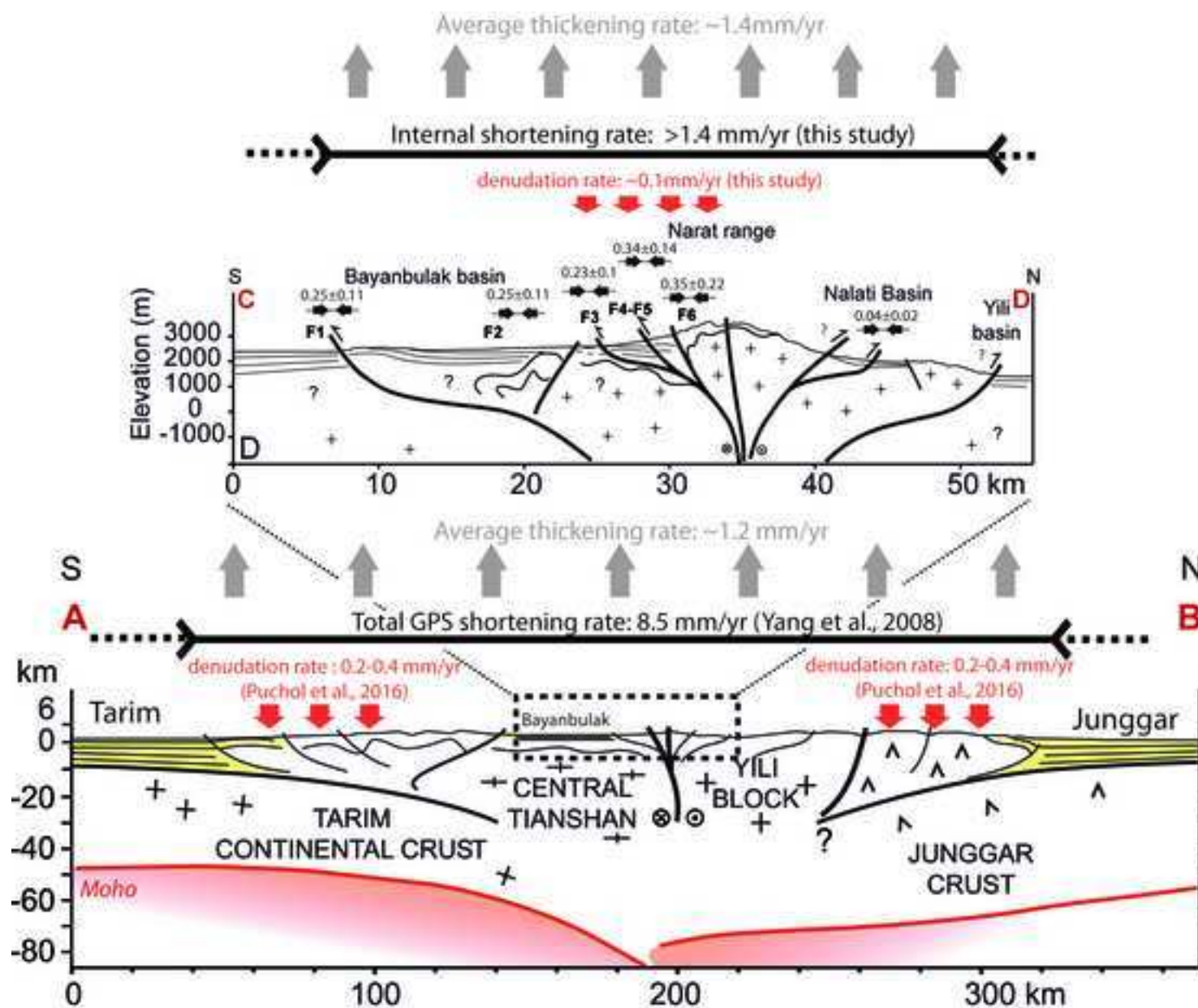


Fig. 8

Supplementary material for online publication only

[Click here to download Supplementary material for online publication only: Online_repository_BBK_final_revised.docx](#)